Fast source optimization involving quadratic line-contour objectives for the resist image

Jue-Chin Yu,[1] Peichen Yu,[1,*] and Hsueh-Yung Chao[2]

[1]*Department of Photonics and Institute of Electro-Optical Engineering, National Chiao-Tung University, Hsinchu, Taiwan*

[2]*ANSYS, Inc., Pittsburgh, Pennsylvania, USA*

**yup@faculty.nctu.edu.tw*

Abstract: In Abbe's formulation, source optimization (SO) is often formulated into a linear or quadratic problem, depending on the choice of objective functions. However, the conventional approach for the resist image, involving a sigmoid transformation of the aerial image, results in an objective with a functional form. The applicability of the resist-image objective to SO or simultaneous source and mask optimization (SMO) is therefore limited. In this paper, we present a linear combination of two quadratic line-contour objectives to approximate the resist image effect for fast convergence. The line-contour objectives are based on the aerial image on drawn edges using a constant threshold resist model and that of pixels associated with an intensity minimum for side-lobe suppression. A conjugate gradient method is employed to assure the convergence to the global minimum within the number of iterations less than that of source variables. We further compare the optimized illumination with the proposed line-contour objectives to that with a sigmoid resist-image using a steepest decent method. The results show a 100x speedup with comparable image fidelity and a slightly improved process window for the two cases studied.

OCIS codes: (110.3960) Microlithography; (100.3190) Inverse problems; (110.1758) Computational imaging; (110.3010) Image reconstruction techniques.

References and links

1. A. E. Rosenbluth, S. Bukofsky, C. Fonseca, M. Hibbs, K. Lai, A. Molless, R. N. Singh, and A. K. K. Wong, "Optimum mask and source patterns to print a given shape," J. Microlithor. Microfabrication. Microsyst. **1**(1), 13–30 (2002).
2. Y. Granik, "Source optimization for image fidelity and throughput," J. Microlithor. Microfabrication. Microsyst. **3**, 509–522 (2004).
3. A. E. Rosenbluth and N. Seong, "Global optimization of the illumination distribution to maximize integrated process window," Proc. SPIE **6154**, 61540H (2006).
4. K. Tian, A. Krasnoperova, D. Melville, A. E. Rosenbluth, D. Gil, J. Tirapu-Azpiroz, K. Lai, S. Bagheri, C.-C. Chen, and B. Morgenfeld, "Benefits and trade-offs of global source optimization in optical lithography," Proc. SPIE **7274**, 72740C, (2009).
5. K. Iwase, P. D. Bisschop, B. Laenens, Z. Li, K. Gronlund, P. V. Adrichem, and S. Hsu, "A new source optimization approach for 2x node logic," Proc. SPIE **8166**, 81662A (2011).
6. Y. Cao, Y. W. Lu, L. Chen, and J. Ye, "Optimized hardware and software for fast, full chip simulation," Proc. SPIE **5754**, 407–414 (2004).
7. S. Geisler, J. Bauer, U. Haak, U. Jagdhold, R. Pliquett, E. Matthus, R. Schrader, H. Wolf, U. Baetz, H. Beyer, and M. Niehoff, "Optical proximity correction for 0.13 μm SiGe:C BiCMOS," Proc. SPIE **6792**, 679210 (2008).
8. L. Pang, P. Hu, D. Peng, D. Chen, T. Cecil, L. He, G. Xiao, V. Tolani, T. Dam, K. H. Baik, and B. Gleason, "Source mask optimization (SMO) at full chip scale using inverse lithography technology (ILT) based on level set methods," Proc. SPIE **7520**, 75200X (2009).
9. I. Torunoglu, E. Elsen, and A. Karakas, "A GPU-based full-chip source-mask optimization solution," Proc. SPIE **7640**, 76401L (2010).

#161845 - $15.00 USD Received 19 Jan 2012; revised 16 Mar 2012; accepted 16 Mar 2012; published 23 Mar 2012

10. S. Jung, W. Sim, M. Jeong, J. Ser, S. Lee, S. W. Choi, X. Zhou, L. Luan, T. Cecil, D. Son, R. Gleason, and D. Kim, "Improving model prediction accuracy for ILT with aggressive SRAFs," Proc. SPIE **7823**, 782311 (2010).
11. C. Lim, V. Temchenko, and M. Niehoff, "Selective inverse lithography methodology," Proc. SPIE **7640**, 764034 (2010).
12. Y. Ping, X. Li, S. Jang, D. Kwa, Y. Zhang, and R. Lugg, "Tolerance-based OPC and solution to MRC-constrained OPC," Proc. SPIE **7973**, 79732M (2011).
13. T. Cecil, C. Ashton, D. Irby, L. Luan, D. H. Son, G. Xiao, X. Zhou, D. Kim, B. Gleason, H. J. Lee, W. J. Sim, M. J. Hong, S. G. Jung, S. S. Suh, and S. W. Lee, "Enhancing fullchip ILT mask synthesis capability for IC manufacturability," Proc. SPIE **7973**, 79731C (2011).
14. Y. Deng, Y. Zou, K. Yoshimoto, Y. Ma, C. E. Tabery, J. Kye, L. Capodieci, and H. J. Levinson, "Considerations in source-mask optimization for logic applications," Proc. SPIE **7640**, 76401J (2010).
15. T. Mülders, V. Domnenko, B. Küchler, T. Klimpel, H. J. Stock, A. A. Poonawala, K. N. Taravade, and W. A. Stanton, "Simultaneous source-mask optimization: a numerical combining method," Proc. SPIE **7823**, 78233X (2010).
16. M. Fakhry, Y. Granik, K. Adam, and K. Lai, "Total source mask optimization: high-capacity, resist modeling, and production-ready mask solution," Proc. SPIE **8166**, 81663M (2011).
17. D. Melville, A. Rosenbluth, K. Tian, K. Lai, S. Bagheri, J. Tirapu-Azpiroz, J. Meiring, S. Halle, G. McIntyre, T. Faure, D. Corliss, A. Krasnoperova, L. Zhuang, P. Strenski, A. Waechter, L. Ladanyi, F. Barahona, D. Scarpazza, J. Lee, T. Inoue, M. Sakamoto, H. Muta, A. Wagner, G. Burr, Y. Kim, E. Gallagher, M. Hibbs, A. Tritchkov, Y. Granik, M. Fakhry, K. Adam, G. Berger, M. Lam, A. Dave, and N. Cobb, "Demonstrating the benefits of source-mask optimization and enabling technologies through experiment and simulations," Proc. SPIE **7640**, 764006 (2010).
18. K. Lai, M. Gabrani, D. Demaris, N. Casati, A. Torres, S. Sarkar, P. Strenski, S. Bagheri, D. Scarpazza, A. E. Rosenbluth, D. O. Melville, A. Wächter, J. Lee, V. Austel, M. Szeto-Millstone, K. Tian, F. Barahona, T. Inoue, and M. Sakamoto, "Design specific joint optimization of masks and sources on a very large scale," Proc. SPIE **7973**, 797308 (2011).
19. J. C. Yu and P. Yu, "Impacts of cost functions on inverse lithography patterning," Opt. Express **18**(22), 23331–23342 (2010).
20. A. Poonawala and P. Milanfar, "Prewrapping techniques in imaging: applications in nanotechnology and biotechnology," Proc. SPIE **5674**, 114–127 (2005).
21. A. Poonawala and P. Milanfar, "OPC and PSM design using inverse lithography: a non-linear optimization approach," Proc. SPIE **6154**, 1159–1172 (2006).
22. A. Poonawala and P. Milanfar, "Mask design for optical microlithography--an inverse imaging problem," IEEE Trans. Image Process. **16**(3), 774–788 (2007).
23. X. Ma and G. R. Arce, "Generalized inverse lithography methods for phase-shifting mask design," Opt. Express **15**(23), 15066–15079 (2007).
24. S. H. Chan, A. K. Wong, and E. Y. Lam, "Initialization for robust inverse synthesis of phase-shifting masks in optical projection lithography," Opt. Express **16**(19), 14746–14760 (2008).
25. N. Jia and E. Y. Lam, "Pixelated source mask optimization for process robustness in optical lithography," Opt. Express **19**(20), 19384–19398 (2011).
26. B. J. Lin, "Optical methods for fine line lithography," in *Fine Line Lithography*, ed. R. Newman (New York: North Holland, 1980).
27. J. C. Yu and P. Yu, "Gradient-based fast source mask optimization (SMO)," Proc. SPIE **7973**, 787320 (2011).
28. M. Born and E. Wolf, *Principles of Optics*, 7th(expanded) ed. (Cambridge University Press, 1999).
29. A. K. Wong, *Optical Imaging in Projection Microlithography* (SPIE Press, 2005).
30. J. W. Goodman, *Introduction to Fourier Optics*, 3rd ed. (McGraw-Hill Science/Engineering/Math, 2005).
31. C. Mack, *Fundamental Principles of Optical Lithography: The Science of Microfabrication* (John Wiley and Sons, 2008).
32. R. C. Gonzalez and R. E. Woods, *Digital Image Processing*, 3rd ed. (Prentice Hall, 2007).
33. D. S. Abrams and L. Pang, "Fast inverse lithography technology," Proc. SPIE **6154**, 534–542 (2006).
34. J. C. Yu, P. Yu, and H. Y. Chao, "Wavefront-based pixel inversion algorithm for generation of subresolution assist features," J. Micro./Nanolith. MEMS MOEMS. **10**, 043014 (2011).
35. S. I. Sayegh, *Image restoration and image design in non-linear optical systems*, PhD Thesis (Univ. of Wisconsin, Madison, 1982).
36. L. N. Trefethen and D. Bau III, *Numerical Linear Algebra* (SIAM, 1997).
37. E. K. P. Chong and S. H. Żak, *An Introduction to Optimization*, 3rd ed. (John Wiley and Sons, 2008).
38. X. Ma and G. R. Arce, "Pixel-based OPC optimization based on conjugate gradients," Opt. Express **19**(3), 2165–2180 (2011).
39. X. Ma and G. R. Arce, "Generalized inverse lithography methods for phase-shifting mask design," Opt. Express **15**(23), 15066–15079 (2007).
40. Y. Shen, N. Jia, N. Wong, and E. Y. Lam, "Robust level-set-based inverse lithography," Opt. Express **19**(6), 5511–5521 (2011).
41. C. Alleaume, E. Yesilada, V. Farys, L. Depre, V. Arnoux, and Z. Li, Y. Trouiller, and A. Serebriakov, "A systematic study of source error in source mask optimization," Proc. SPIE **7823**, 782312, 782312-7 (2010).
42. T. Matsuyama, N. Kita, T. Nakashima, O. Tanitsu, and S. Owa, "Tolerancing analysis of customized illumination for practical applications of source and mask optimization," Proc. SPIE **7640**, 764007, 764007-10 (2010).

#161845 - $15.00 USD Received 19 Jan 2012; revised 16 Mar 2012; accepted 16 Mar 2012; published 23 Mar 2012

43. L. Xu, X. Peng, Z. Guo, J. Miao, and A. Asundi, "Imaging analysis of digital holography," Opt. Express **13**(7), 2444–2452 (2005).
44. I. Moon and B. Javidi, "Shape tolerant three-dimensional recognition of biological microorganisms using digital holography," Opt. Express **13**(23), 9612–9622 (2005).
45. D. J. Brady, K. Choi, D. L. Marks, R. Horisaki, and S. Lim, "Compressive holography," Opt. Express **17**(15), 13040–13049 (2009).
46. S. Tamulevicius, A. Guobiene, G. Janusas, A. Palevicius, V. Ostasevicius, and M. Andrulevicius, "Optical characterization of diffractive optical elements replicated in polymers," J. Microlithor. Microfabrication. Microsyst. **5**, 013004 (2006).
47. G. D. M. Jeffries, G. Milne, Y. Zhao, C. Lopez-Mariscal, and D. T. Chiu, "Optofluidic generation of Laguerre-Gaussian beams," Opt. Express **17**(20), 17555–17562 (2009).

1. Introduction

In recent years, source optimization (SO) and mask optimization (MO) have attracted great interests among semiconductor foundries and equipment vendors because of its capability for further extending the life of 193-nm optical lithography [1–13]. With the availability of free-form sources using diffractive optical elements (DOE), SO serves as a new option for achieving higher resolution without increasing the complexity of mask design. The proposal of source mask co-optimization (SMO) further permits the exploration of design spaces for both illuminations and masks [14–18]. Since both SO and MO rely on the complexity of computational lithography algorithms to explore all possible solutions, the design of objective functions has a significant impact on the quality of developed patterns [19], the manufacturability of sources and masks, and the convergence. It is also desirable to use the same objective functions for simultaneous SMO.

In the past, the resist-image objective based on a sigmoid transformation of the aerial image has been extensively used to approximate the resist effect in optical microlithography, particularly for mask correction due to its unique contour-aware property [20–25]. The logarithmic sigmoid function has the advantage of being differentiable and its parameters are adjustable according to the sensitivity of photoresists. However, such objective with a functional form precludes the formulation of SO into a linear or quadratic problem using Abbe's formulation, as well as to the implementation of simultaneous SMO using the same cost function. Therefore, the conventional approach for the resist-image objective is not desirable due to an increased computational time and probability of local minimum traps, as also seen in MO. To circumvent such problems, Chan et al. have proposed a projection-based active set method to improve the convergence [24].

Generally speaking, if the associated objective functions have a quadratic form, the SO algorithm can be rather efficient and exhibits a global minimum. To reach a compromise between speed and image fidelity, the cost function of SO often involves a quadratic aerial-image objective function with specific weightings for contour pixels (or similar techniques) to account for the photoresist effect. The complexity therefore arises since the result is not exactly the same as the resist-image function in terms of side-lobe suppression. Moreover, tuning of the weighting coefficients is also not straightforward. Hence the applicability of such kinds of cost functions to SO and SMO is also rather limited.

In this paper, we present a linear combination of two quadratic line-contour objectives to approximate the resist image effect. Our goal is to reduce the computational cost when the resist-image objective are involved in SO. The line-contour objectives are based on the aerial image on drawn edges using a constant threshold resist (CTR) model and that of pixels associated with an intensity minimum for side-lobe suppression [26]. It can also be derived that the former is a piecewise linear approximation of the sigmoid function on the drawn edges. As a result, we are able to simplify the SO problem using quadratic programming. A conjugate gradient method is then employed to assure the convergence to the global minimum within the number of iterations less than that of source variables. We further compare the optimized

#161845 - $15.00 USD Received 19 Jan 2012; revised 16 Mar 2012; accepted 16 Mar 2012; published 23 Mar 2012

illumination with the proposed line-contour objectives to that with a sigmoid resist-image using a steepest decent method. The results show a 100x speedup with comparable image fidelity and a slightly improved process window for the two cases studied.

In Section 2, we will review the image formation in a partially coherent system and introduce the illumination cross coefficient (ICC) [27], which simplifies the forward imaging calculation and serves as a foundation for the formulation of cost functions. We further analyze why the nonlinear sigmoid function in conjunction with the CG method may take longer iterations to converge. However, the problem no longer exists in quadratic line-contour cost functions. The formulations are then applied for source optimization of contact arrays in Section 3. We will demonstrate that the line-contour objectives in conjunction with CG is capable of achieving 100x speedup over the traditional approach, i.e. the sigmoid-based steepest descent, without compromising image fidelity and process windows.

2. Methodology

2.1 Image formation model

Lithography images, or so-called aerial images, can be simulated by Abbe's method [28, 29] which integrates the images formed by all source points incoherently as Eq. (1).

$$I(x,y)=\int\int_{-\infty}^{\infty} J(u,v) \left[\left|\int\int_{-\infty}^{\infty} H(u+u',v+v')M(u',v')e^{-i2\pi[u'x+v'y]}du'dv'\right|^2\right]dudv, \tag{1}$$

where (x, y) and (u, v) denote the spatial coordinates and spatial frequencies of a mask, respectively. $J(u, v)$ is the strength of the point source located at (u, v) [29], $H(u, v)$ is the optical system transfer function, and $M(u, v)$ is the mask spectrum.

The optical system is band-limited [30], so the transfer function $H(u,v)$ can be described by a low-pass filter as Eq. (2).

$$\begin{cases} H(u,v)=1, \sqrt{u^2+v^2}\le\dfrac{NA}{\lambda}, \\ H(u,v)=0, otherwise, \end{cases} \tag{2}$$

where NA/λ is the cut-off frequency of the optical system, NA is the numerical aperture which limits the largest oblique angle of rays forming the aerial image, and λ is the working wavelength.

In a partially coherent system, the finite source $J(u,v)$ in Eq. (3) is limited by the coherent factor σ ($0<\sigma\le1$) [29, 31].

$$\begin{cases} J(u,v)\ge 0, \sqrt{u^2+v^2}\le\sigma\dfrac{NA}{\lambda}, \\ J(u,v)=0, otherwise. \end{cases} \tag{3}$$

The spectral integral in the bracket of Eq. (1) is the ICC

$$ICC(x,y;u,v)=\left|\int\int_{-\infty}^{\infty} H(u+u',v+v')M(u',v')e^{-i2\pi[u'x+v'y]}du'dv'\right|^2. \tag{4}$$

#161845 - $15.00 USD Received 19 Jan 2012; revised 16 Mar 2012; accepted 16 Mar 2012; published 23 Mar 2012

Because *ICC* represents the image formed by a unit source with spatial frequencies (u,v), Eq. (1) can be interpreted as a linear superposition of images with coefficients $J(u,v)$.

For computing pixelated images, Eq. (1) should be discretized as

$$\mathrm{I}(i,\, j) = \sum_{k=1}^{S}\sum_{l=1}^{S} \mathrm{J}(k,l)\mathrm{ICC}(i,\, j; k, l), \quad i,\, j = 1, 2, ..., N. \tag{5}$$

The variables i, j, k, and l denote the indices of discretized x, y, u, and v. N and S are the total sample numbers in spatial and spectral domains, respectively. Likewise the *ICC* in Eq. (4) can be discretized as

$$\mathrm{ICC}(i,\, j; k, l) = \Big|\ \sum_{k'=1}^{S}\sum_{l'=1}^{S} \mathrm{H}(k+k', l+l')\mathrm{M}(k', l')e^{-i2\pi\left[u'(k,l)x(i,j)+v'(k,l)y(i,j)\right]}\ \Big|^2. \tag{6}$$

To simplify the matrix computation, the 2-D discrete source in Eq. (5) can be converted to a 1-D vector and ICC in Eq. (6) can be expressed by a 2-D matrix. Consequently the output image is also a 1-D vector that can be converted to a 2-D distribution by rearranging the rank. Thus Eq. (5) can be represented as Eq. (7).

$$\mathbf{I} = \mathbf{ICC}\ \mathbf{J}, \tag{7}$$

where the sizes of **I**, **J**, and **ICC** are $N^2 \times 1$, $S^2 \times 1$, and $N^2 \times S^2$, respectively. Figure 1 illustrates the aforementioned matrix operations.

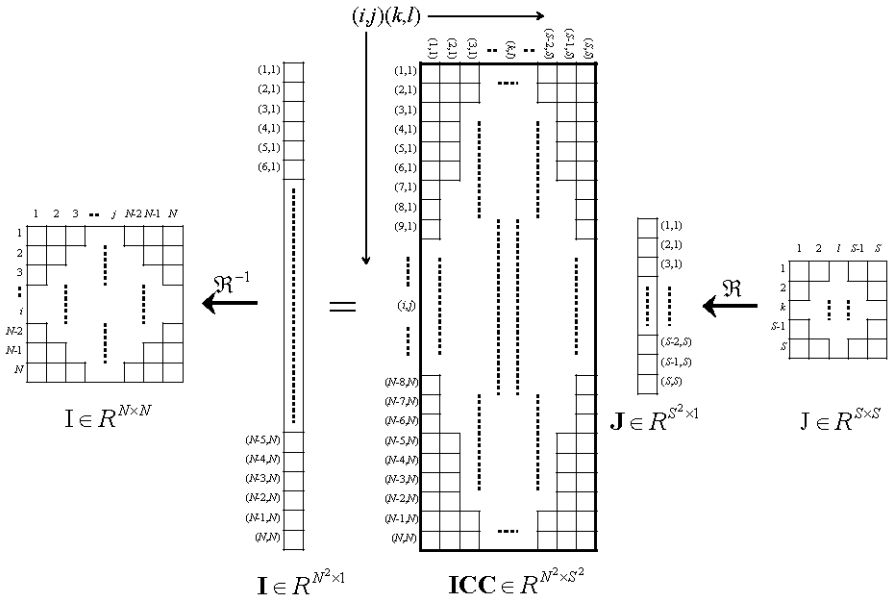

Fig. 1. Illustration of the matrix operations in Eq. (7). $\Re$ denotes the matrix to vector conversion. $\Re^{-1}$ denotes the vector to matrix conversion.

As a result, every row of the **ICC** matrix composes of one spatial image point by summing all row elements with the coefficients in **J**. To obtain the target image points, only the relative rows are required to be extracted from **ICC** for the computation. Thus **ICC** can be partitioned to several parts for different image configurations. For example, the images may be classified into the marginal and face parts. The former preserves the high spatial frequency fidelity and the latter controls the low spatial frequency response. Figure 2 illustrates the operations of image

#161845 - $15.00 USD Received 19 Jan 2012; revised 16 Mar 2012; accepted 16 Mar 2012; published 23 Mar 2012

formation of different parts. As an example, in Fig. 2(a) the inside marginal pixels are painted in light grey, outside marginal pixels in grey, and surrounding face pixels in black. The surrounding face pixels prevent the non-patterned images to be printed. For a dark-field binary intensity mask, the inside marginal pixels are the marginal pixels with value 1. On the contrary, the outside marginal pixels are the marginal pixels with value 0. The inside and outside marginal pixels can be found by using the *Laplacian* operator [32] for masks with arbitrary patterns. In Fig. 2(b), the combinations of rows extracted from **ICC** form the new sub-**ICCs** for different image configurations. The light grey, grey and black color bands denote the rows corresponding to the pixels in Fig. 2(a). Finally in Fig. 2(c), the matrix operations represent the image formation of the combined images.

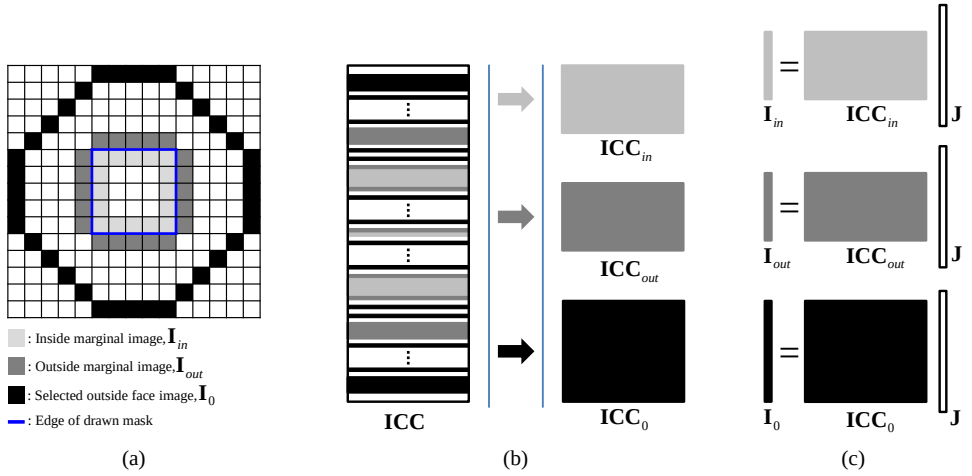

Fig. 2. Partitioned ICC for different parts of image formation. (a) Example of a pixelated square contact mask. (b) Row extractions and sub-ICC generation. (c) Matrix operations of various image formations by using sub-ICCs.

2.2 Cost functions

To find the optimal source, the proper objective functions for quantifying the deviation between ideal designs and real simulations should first be defined. In general the final resist images under the CTR model are the uppermost concern. However, the resist images are usually simulated by the nonlinear *sigmoid* function [20–22], which destroys the benefit of linear operations in Abbe's image formation. The sigmoid function has the form as Eq. (8).

$$T(\mathbf{I}) = \frac{1}{1+e^{-a(\mathbf{I}-tr)}} = \frac{1}{1+e^{-a(\mathbf{ICC\,J}-tr)}}, \tag{8}$$

where a characterizes the sensitivity of the photoresist and controls the slopes of sidewall profiles.tr is the parameter of the constant threshold level. The objective function using Eq. (8) is defined as Eq. (9).

$$F_{Sigmoid} = \left\| T(\mathbf{I}_t) - T(\mathbf{I}) \right\|^2, \tag{9}$$

where $\|\cdot\|$ is the operation of *Euclidean* norm. $\mathbf{I}_t$ is the target aerial image which can be elaborately designed according to the geometric shapes of patterns [19, 33, 34].

#161845 - $15.00 USD Received 19 Jan 2012; revised 16 Mar 2012; accepted 16 Mar 2012; published 23 Mar 2012

Two objective functions are designed to have quadratic forms and to achieve the same accuracy as the nonlinear sigmoid function. One is the threshold-intensity only awareness and another is non-pattern region monitoring. The first can be formulated as

$$F_R = \left\| \frac{1}{2}\left(\mathbf{ICC}_{in} + \mathbf{ICC}_{out}\right)\mathbf{J} - tr \right\|^2, \tag{10}$$

where the sizes of $\mathbf{ICC}_{in}$ and $\mathbf{ICC}_{out}$ are both $N' \times S^2$ and N' denote the number of pixels on the margins of drawn patterns.

From another point of view, Eq. (10) only monitors the cost on drawn edges regardless of other places. Such formulation has been used by Sayegh for image design [35]. In a sense, Eq. (10) is not sensitive to image slopes for matching the sigmoid characteristic in the transition region. The differences in image slopes in the edge positions do not contribute to the deviation in costs for both cases.

To suppress the image in non-pattern regions, the images of closed curves surrounding the drawn features are incorporated into optimization. Such curves whose widths are one pixel are like the one composed of the black pixels in Fig. 2(a). A large amount of non-pattern images leads to low yield due to undesired resist images, or so-called side-lobes. Therefore, the objective function for side-lobe printing can be designed as

$$F_0 = \left\| \mathbf{ICC}_0\ \mathbf{J} - \delta \right\|^2, \tag{11}$$

where δ is chosen to be as small as possible, but should remain positive. The size of $\mathbf{ICC}_0$ is $N'' \times S^2$, where N'' denotes the number of chosen pixels surrounding the drawn patterns.

The distance of every surrounding pattern is half a pitch for periodic patterns and $0.61\lambda/NA$ for isolated and semi-isolated patterns. The half-pitch is associated with the minimum intensity of periodic patterns. $0.61\lambda/NA$ is associated with the first minimum of diffractive patterns for a circular aperture. Moreover, the sigmoid function acts as a high pass filter where the images will be converted to 0 or 1 beyond the transition region. Such conversion is highly nonlinear. Equation (11) cannot simulate well, but has a similar trend that prefers to suppress side-lobe printing for minimizing F_0.

By defining objective functions on critical parts of the image and reformulating the sigmoid-based cost function as a line-contour objective, the computational cost of SO is significantly reduced.

2.3 Optimization

In terms of matrix operation, Eqs. (10) and (11) can be rewritten as Eqs. (12) and (13).

$$F_R = \left(\frac{1}{2}\left(\mathbf{ICC}_{in} + \mathbf{ICC}_{out}\right)\mathbf{J} - \mathbf{tr}\right)^{\mathrm{T}} \left(\frac{1}{2}\left(\mathbf{ICC}_{in} + \mathbf{ICC}_{out}\right)\mathbf{J} - \mathbf{tr}\right), \tag{12}$$

$$F_0 = (\mathbf{ICC}_0\ \mathbf{J} - \boldsymbol{\delta})^{\mathrm{T}} (\mathbf{ICC}_0\ \mathbf{J} - \boldsymbol{\delta}), \tag{13}$$

where T denotes transpose operation, $\mathbf{tr} = tr \times [1,\ldots,1]^{\mathrm{T}}$, and $\boldsymbol{\delta} = \delta \times [1,\ldots,1]^{\mathrm{T}}$. The sizes of $\mathbf{tr}$, and $\boldsymbol{\delta}$ are $N' \times 1$, and $N'' \times 1$, respectively. Thus the overall cost of the line-contour objectives is obtained by linearly superposing F_R, and F_0 with the coefficients c_1, and c_2 as Eq. (14):

$$F_{Linear} = c_1 F_R + c_2 F_0. \tag{14}$$

#161845 - $15.00 USD Received 19 Jan 2012; revised 16 Mar 2012; accepted 16 Mar 2012; published 23 Mar 2012

Consequently, by minimizing Eq. (14) with an argument **J**, we can find the optimal source $\hat{\mathbf{J}}$ as Eq. (15):

$$\hat{\mathbf{J}} = \arg\min_{\mathbf{J}} .\{F_{Linear}\}. \tag{15}$$

Moreover, Eq. (14) can be expanded to have a quadratic form as Eq. (16).

$$F_{Linear} = \mathbf{J}^{\mathrm{T}}\mathbf{Q}\mathbf{J} - \mathbf{b}^{\mathrm{T}}\mathbf{J} + c, \tag{16}$$

where

$$\mathbf{Q} = \frac{c_1}{4}\left(\mathbf{ICC}_{in} + \mathbf{ICC}_{out}\right)^{\mathrm{T}}\left(\mathbf{ICC}_{in} + \mathbf{ICC}_{out}\right) + c_2\mathbf{ICC}_0^{\mathrm{T}}\mathbf{ICC}_0, \tag{17}$$

$$\mathbf{b} = c_1\left(\mathbf{ICC}_{in} + \mathbf{ICC}_{out}\right)^{\mathrm{T}}\mathbf{tr} + 2c_2\mathbf{ICC}_0^{\mathrm{T}}\boldsymbol{\delta}, \tag{18}$$

$$c = c_1\mathbf{tr}^{\mathrm{T}}\mathbf{tr} + c_2\boldsymbol{\delta}^{\mathrm{T}}\boldsymbol{\delta}. \tag{19}$$

The sizes of **Q**, **b** and c in Eqs. (17), (18), and (19) are $S^2 \times S^2$, $S^2 \times 1$, and 1×1, respectively. Because the overall cost function is quadratic, the optimal source $\hat{\mathbf{J}}$ is guaranteed to be found by conjugate-gradient (CG) method with no more than S^2 iterations [36,37]. The algorithm can be summarized by the pseudo-code in Table 1.

Table 1. Pseudo-Code of CG

Algorithm 1. SO by CG
Input:
Load initial source $\mathbf{J}^{(0)}$. Set $k = 0$.
Calculation:
1. $\mathbf{g}^{(0)} = \nabla_{\mathbf{J}}F_{Linear}(\mathbf{J}^{(0)})^{\dagger}$. If $\|\mathbf{g}^{(0)}\| < \varepsilon$ [‡], stop; else, set $\mathbf{d}^{(0)} = -\mathbf{g}^{(0)}$.
2. $\alpha_k = -(\mathbf{g}^{(k)\mathrm{T}}\mathbf{d}^{(k)})/(\mathbf{d}^{(k)\mathrm{T}}\mathbf{Q}\mathbf{d}^{(k)})$.
3. $\mathbf{J}^{(k+1)} = \mathbf{J}^{(k)} + \alpha_k\mathbf{d}^{(k)}$.
4. Set all negative entries of $\mathbf{J}^{(k+1)}$ are equal to 0.
5. $\mathbf{g}^{(k+1)} = \nabla_{\mathbf{J}}F_{Linear}(\mathbf{J}^{(k+1)})$. If $\|\mathbf{g}^{(k+1)}\| < \varepsilon$, stop; Set $\hat{\mathbf{J}} = \mathbf{J}^{(k+1)}$.
6. $\beta_k = (\mathbf{g}^{(k+1)\mathrm{T}}\mathbf{Q}\mathbf{d}^{(k)})/(\mathbf{d}^{(k)\mathrm{T}}\mathbf{Q}\mathbf{d}^{(k)})$.
7. $\mathbf{d}^{(k+1)} = -\mathbf{g}^{(k+1)} + \beta_k\mathbf{d}^{(k)}$. Set $k = k + 1$; Go to step 2.
Output:
Export optimal source $\hat{\mathbf{J}}$.

[†] $\mathbf{g} = 2(\mathbf{QJ} - \mathbf{b})$. $\nabla_{\mathbf{J}} = [\partial/\partial\mathbf{J}(1,1), \partial/\partial\mathbf{J}(2,1), \ldots, \partial/\partial\mathbf{J}(S,S)]^{\mathrm{T}}$.

[‡] ε is an extremely small value, but positive.

Furthermore, to verify the effectiveness of our algorithm, the SO results by sigmoid model are also calculated. Likewise the optimal source by sigmoid model $\hat{\mathbf{J}}'$ in Eq. (20) can be defined as an argument for minimizing Eq. (9) and like Eq. (15).

$$\hat{\mathbf{J}}' = \arg\min_{\mathbf{J}} .\{F_{Sigmoid}\}. \tag{20}$$

#161845 - $15.00 USD Received 19 Jan 2012; revised 16 Mar 2012; accepted 16 Mar 2012; published 23 Mar 2012

However, Eq. (9) is not in quadratic form. The algorithm presented in Table 1 is not applicable. Although several modified CG methods have been proposed to address non-quadratic problems [37], there are two drawbacks limiting the application of CG in high-order problems. First, the Step 2 in Table 1 that decides α_k is a time-consuming one dimension optimization problem [37,38]. Second, β_k in Step 6 of Table 1 approximated by a quadratic function is not accurate enough to characterize the nonlinearity of the sigmoid model. That leads to extra iterations for converging.

Thus the steepest-descent (SD) algorithm [37] widely used in inverse mask optimization with sigmoid resist images [19,22,39,40] is performed to compute $\hat{\mathbf{J}}'$. Table 2 summarizes the steps of the SD algorithm.

Table 2. Pseudo-Code of SD

Algorithm 2. SO by SD

Input:

Load initial source $\mathbf{J}^{(0)}$. Set $k = 0$.

Calculation:

1. $\mathbf{g}'^{(k)} = \nabla_{\mathbf{J}} F_{Sigmoid}(\mathbf{J}^{(k)})^{\dagger}$.
2. $\mathbf{J}^{(k+1)} = \mathbf{J}^{(k)} + \gamma\, \mathbf{g}'^{(k)}$.
3. Set all negative entries of $\mathbf{J}^{(k+1)}$ are equal to 0.

   If $F_{Sigmoid}(\mathbf{J}^{(k+1)}) > F_{Sigmoid}(\mathbf{J}^{(k)})$, $\gamma = \alpha'\gamma$[§]; Set $\mathbf{J}^{(k+1)} = \mathbf{J}^{(k)}$.

   Elseif $F_{Sigmoid}(\mathbf{J}^{(k)}) - F_{Sigmoid}(\mathbf{J}^{(k+1)}) < \varepsilon$ [‡], stop; Set $\hat{\mathbf{J}}' = \mathbf{J}^{(k+1)}$.

Else set $k = k + 1$; Go to step 1.

Output:

Export optimal source $\hat{\mathbf{J}}'$.

[†] $\mathbf{g}' = -2a\mathbf{ICC}^{\mathrm{T}}[(T(\mathbf{I}_t)-T(\mathbf{I}))\cdot(1-T(\mathbf{I}))\cdot T(\mathbf{I})]$. $\cdot$ is the pixel-wise multiplication. $\nabla_{\mathbf{J}} = [\partial/\partial\mathbf{J}(1,1), \partial/\partial\mathbf{J}(2,1), \ldots, \partial/\partial\mathbf{J}(S,S)]^{\mathrm{T}}$.

[§] $\alpha' < 1$. $\gamma = 5$ and $\alpha' = e^{-0.5}$ in our work.

[‡] ε is an extremely small value, but positive.

Because only the source variables within the circle with the $\sigma NA/\lambda$ radius are available, the total source number is approximately equal to $S^2 \times \pi/4$. Therefore, there are $2 \times (S^2 \times \pi/4)^2$ and $2 \times N^2 \times (S^2 \times \pi/4)$ multiplications in every CG and SD iteration, respectively. Hence, the computational complexities of SO by CG and SD incorporating line-contour objectives and sigmoid-based resist image costs are $O((S^2 \times \pi/4)^2 \times K_{CG})$ and $O(N^2 \times (S^2 \times \pi/4) \times K_{SD})$, respectively,where K_{CG} and K_{SD} are iteration numbers of CG and SD. Theoretically the elapsed time t of computation is proportional to the complexity and the speed t^{-1} is inversely proportional to the elapsed time t. Thus the speed ratio of CG comparing to SD is t_{SD}/t_{CG} which can be formulated as $\kappa_1 \times N^2/(S^2 \times \pi/4) \times K_{SD}/K_{CG}$. κ_1 is a constant which depends on the programming efficiency of different algorithms. Usually $N^2/(S^2 \times \pi/4)$ and K_{SD}/K_{CG} are both much larger than one, which implies CG being a more efficient approach.

Finally we define the functions $\mathrm{DoPE}_{\mathrm{J}}$ and $\mathrm{DoPE}_{\mathrm{I}}$ in Eqs. (21) and (22) to quantify the difference between sources and aerial images, respectively, where DoPE stands for the degree of pattern error.

$$\mathrm{DoPE}_{\mathrm{J}} = \frac{1}{2}\sum\left|\frac{\mathbf{J}_2}{\sum\mathbf{J}_2} - \frac{\mathbf{J}_1}{\sum\mathbf{J}_1}\right|, \quad \mathbf{J}_1, \mathbf{J}_2 \geq 0. \tag{21}$$

$$\mathrm{DoPE}_{\mathrm{I}} = \frac{1}{2}\sum\left|\frac{\mathbf{I}_2}{\sum\mathbf{I}_2} - \frac{\mathbf{I}_1}{\sum\mathbf{I}_1}\right|, \quad \mathbf{I}_1, \mathbf{I}_2 \geq 0. \tag{22}$$

By this way, the DoPEs are in the range of [0, 1].

#161845 - $15.00 USD Received 19 Jan 2012; revised 16 Mar 2012; accepted 16 Mar 2012; published 23 Mar 2012

3. Results and discussion

The source and drawn mask templates are composed of 65 × 65 and 256 × 256 pixels with S and N equal to 65 and 256, respectively. The pixel size is 2.48x2.48 nm^2. Two demo mask configurations are regular and brick contact arrays as shown in Fig. 3. In our simulations, c1/c2 ratios are set to be 3.28 and 6 for the two masks, respectively. The surrounding pixels for side-lobe checking are placed in the distance of half pitch from the center of every contact on the masks with a and δ equal to 90 and 0, respectively. The illumination and projection system have working wavelength λ, numerical aperture NA and coherent factor σ equal to 193 nm, 1.35 and 0.9, respectively. In order to make a fair comparison, all images are normalized by integration of a full-open source with unit intensity and blank mask. The threshold tr is chosen to be 0.5 after comprehensive studies. However, in the real-world situation, the threshold should be fine-tuned to match the wafer data before any correction. Moreover, the strength of every variable in following optimal sources involves exposure-time (dose) and intensity (power-per-unit-mask-area). Thus the dose is adjustable like a convention illuminator because a large dose means a low intensity of the source variable when we keep the strength constant.

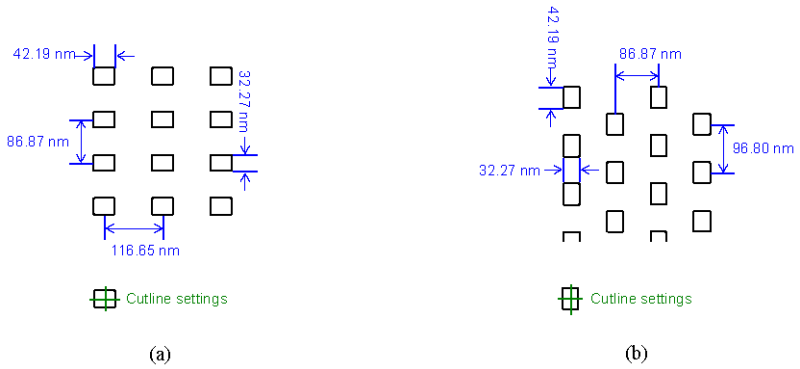

Fig. 3. (a) Regular contact array and (b) Brick contact array used for source optimization.

Figure 4 illustrates the experimental results using the contact array in Fig. 3(a). The source coordinates are normalized by $\sigma NA/\lambda$. The optimal sources of both models are very close. There are four energy poles which are approximately at ± 60° and ± 120° in both optimal sources. Similarly, Fig. 5 shows the experimental results using the contact array in Fig. 3(b). Both sources are quite similar and have six energy poles near ± 30°, ± 90°, and ± 150°. The poles where energy is concentrated generate interfered spatial frequencies which match the spatial distribution of masks. The places besides poles are background parts that have a few deviations between both optimal sources. Such parts provide near constant intensity distributions for basis that biases the vibrations interfered by poles across the threshold tr. Moreover, our patterns include not only the repetitive parts of periodic patterns, but also the marginal parts. Thus they can be seen as a finite periodic structure. To hold the pattern fidelity in periodic (center) and aperiodic (margin) parts, the final optimal sources will have strong background intensities if there is no other constraint. However, adding constraints to our cost functions will increase the challenges to have the similar optimal sources in our work due to extra tunable parameters. Because our main goal is to demonstrate that similar optimal sources will be obtained using different cost functions, such issue is not a major concern of our work. Additionally, the low contrast images will be obtained as a source optimized for various structures. Such low contrast usually results from the center parts of the sources.

As a result, our line-contour objectives can simulate the resist image costs well using Eq. (10) while the image intensity is near the threshold. The threshold-only awareness

#161845 - $15.00 USD Received 19 Jan 2012; revised 16 Mar 2012; accepted 16 Mar 2012; published 23 Mar 2012

characteristic of Eq. (10) is sensitive to the average intensity of the two adjacent pixels in and out the drawn edges. Therefore, no matter how sharp the image slops are in drawn edges, the costs are the same when the drawn edge image intensities have no change. That is consistent with sigmoid model that any image intensity of two adjacent pixels across *tr* will be converted to just 1 or 0. Nevertheless the images away from drawn edge locations have some deviations as using Eq. (11). Such results are predictable because Eq. (11) only forces the intensity of the surrounding rings to δ, that is not like sigmoid as a high pass filter. Moreover, Eq. (9) shows that the cost of any image intensity above (or below) *tr* is equal in one location, but Eq. (11) does not. Furthermore, every drawn pattern has only one side-lobe checking ring whose monitoring ranges are much smaller than the sigmoid model.

In terms of images, they also show similar threshold contours, where the magenta and green curves are associated with sigmoid-based resist image costs and line-contour objectives approaches, respectively. Moreover, the overall image qualities are excellent after SO although the patterns are still not on the target (black curves), but close. Such results relieve the load of MO and lead to simpler OPC masks.

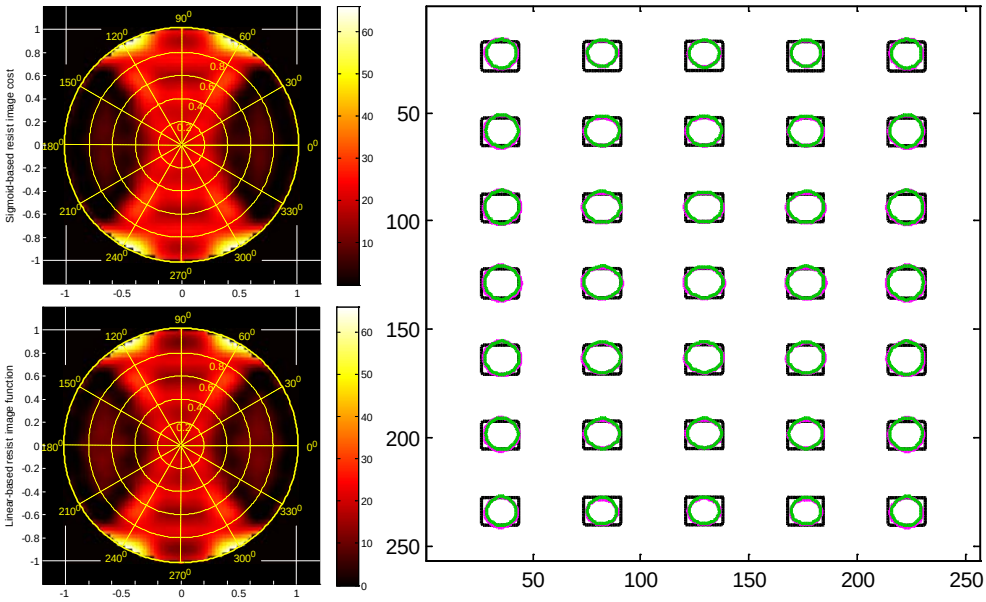

Fig. 4. Optimal sources of the regular contact array in Fig. 3(a).

#161845 - $15.00 USD Received 19 Jan 2012; revised 16 Mar 2012; accepted 16 Mar 2012; published 23 Mar 2012

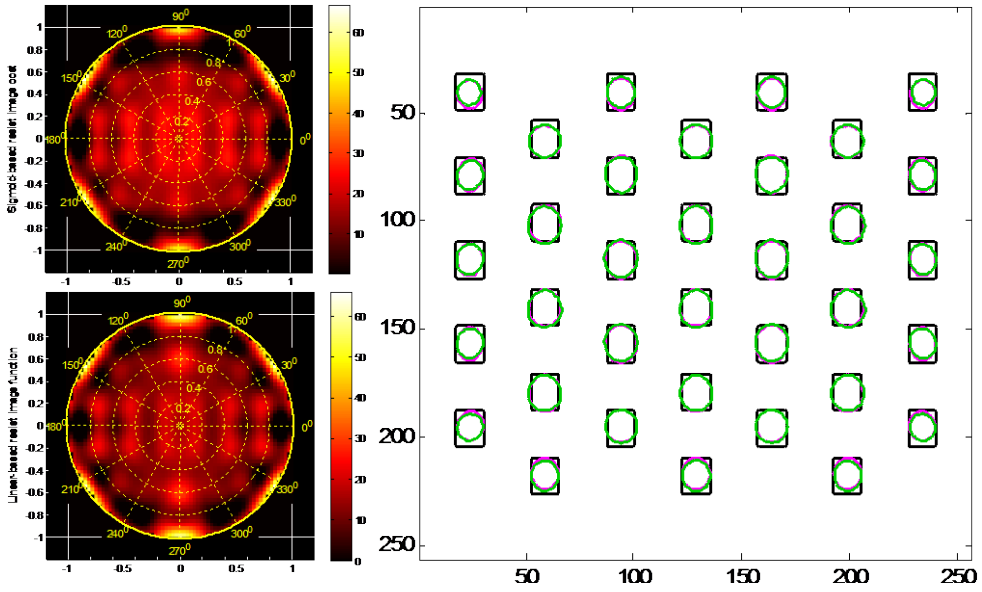

Fig. 5. Optimal sources of the brick contact array in Fig. 3(b).

Finally we quantize the similarity of different optimal sources and their images by using Eqs. (21) and (22). The average edge placement errors (EPEs) and normalized image log slopes (NILSs) are also calculated according to cutline settings in Fig. 3(a) and 3(b).

In Table 3, the average EPEs of both mask structures using two different resist image cost functions are close and near the pixel size. Likewise average NILSs are also close. Moreover, $DoPE_J$ of both masks are 5.24% and 10.87%, which implies the optimal sources using two resist image cost functions are highly similar. Although $DoPE_J$s of both masks are more than 5%, $DoPE_I$s are less than 2%. Such phenomenon indirectly verifies that aerial images are quite insensitive to large defects on sources [41, 42]. The above merit matches one of the characteristics of holograms that 3D images are reproduced well even some parts are damaged [43–45]. In fact the diffraction optical element (DOE), one of the techniques for generating the free form sources, is based on holography [46, 47].

Table 3. Measurements of Sources and Aerial Images

Measurement / Mask; Resist image cost		EPE (nm)	NILS (AU)	$DoPE_J$ (%)	$DoPE_I$ (%)
Regular contact array	Sigmoid	2.75	1.49	5.24	1.11
	Line-contour	1.93	1.18		
Brick contact array	Sigmoid	2.58	1.25	10.87	1.22
	Line-contour	2.44	1.13		

After verifying sources and images obtained from two resist image cost functions are the same, the next step is to check their impact on the speed of source optimization. Table 4 lists the relative analyses and measurements.

As a result, our line-contour objectives with CG take much less iteration than the sigmoid model with SD. The complexity ratio is evaluated by $N^2/(S^2 \times \pi/4) \times K_{SD}/K_{CG}$ as mentioned in the previous section and $N^2/(S^2 \times \pi/4)$ is 19.75 in our settings. The complexity ratios are up to hundreds. Therefore, the speeds are enhanced by two orders. Moreover, the complexity ratios

#161845 - $15.00 USD Received 19 Jan 2012; revised 16 Mar 2012; accepted 16 Mar 2012; published 23 Mar 2012

and speedup ratios of both masks are in the relation of a constant κ_1 whose values are 0.65 and 0.62 for regular and brick contact arrays, respectively. Such consistent value of κ_1 for both masks implies the parameters for estimating speeds from complexity formulas have been entirely taken into consideration.

Table 4. Evaluation of Computational Complexity and Speed Enhancement

Mask; Resist image cost \ Measurement		Iteration number (K)	Complexity Ratio ($19.75 \times K_{Sig}/K_{Lin}$)	Speed up Ratio $(t^{-1})_{Lin}/(t^{-1})_{Sig}$	κ_1
Regular contact array	Sigmoid	386	162.20	105.98	0.65
	Line-contour	47			
Brick contact array	Sigmoid	550	293.58	182.34	0.62
	Line-contour	37			

Moreover, process variations of different optimal sources of each mask are also evaluated. Process variations are important to yields and expected to have close trends if similar sources are used. The exposure-defocus (E-D) process window (PW) is the main metric to characterize the process variations. Figure 6 shows the average E-D PWs of both masks using sigmoid-based and our line-contour objectives. Due to the sub-wavelength CD and pitch, the effective E-D PWs are within *Kirchhoff* diffraction region [31] where the defocus is smaller than half wavelength. In Fig. 6(a) the average E-D curves match well within the ± 15 nm defocus range. Though the average E-D curves in Fig. 6(b) have more misalignments, they are still in the similar trends which are concave parabolas. Such results are reasonable because the $DoPE_J$ of the brick contact array is more than that of the regular contact array.

In summary, source differences reveal obvious impacts with the increasing propagation distance from nominal points. Such propagation let the image deviations spread from points to spots whose covering areas become wide with far propagating distances. Therefore, the threshold image contours formed by different optimal sources in defocus positions suffer from different impacts of places other than target margins. Consequently, the farther the defocus, the more deviations are from other places because spots become broader. Such different impacts of source variations result from Eq. (11) not matching well with sigmoid model as previously mentioned. Furthermore, our SOs are based on nominal models, so the average E-D curves of both cost functions overlap near the 0 nm defocus position.

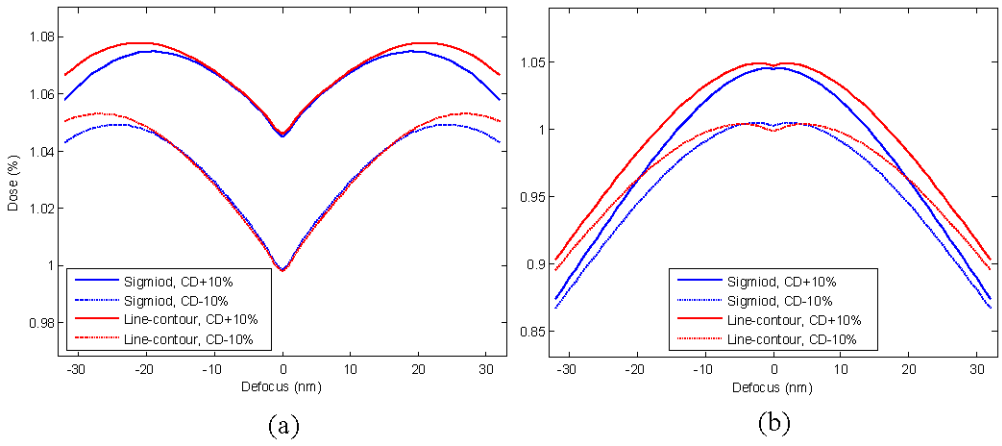

Fig. 6. Average E-D PW of (a) Regular contact array, and (b) Brick contact array.

#161845 - $15.00 USD Received 19 Jan 2012; revised 16 Mar 2012; accepted 16 Mar 2012; published 23 Mar 2012

In Table 5 we tabulate the representative measurements of E-D PWs in Fig. 6. The DoF and ΔDose are measured by finding the optimal ellipse that is tangent with the curves and having the maximum area. Thus the horizontal and vertical axes are DoF and ΔDose, respectively. Such measurements show better elliptic E-D PWs as using our line-contour objectives, especially in brick contact array. Finally, small values ($<10^{-2}$) of standard deviations of blue and red curves in Figs. 6 (a) and 6(b) quantitatively verify the similarity between process variation trends. As we previously discussed, the brick contact array has larger standard deviation because it suffers more from the deviation of source differences.

Table 5. Measurements of E-D PWs

Measurement / Mask; Resist image cost		E-D PW (Ellipse)		Standard deviation of
		DoF (nm)	ΔDose (%)	E-D curves
Regular contact array	Sigmoid	17.21	3.01	0.003
	Line-contour	18.36	3.13	
Brick contact array	Sigmoid	18.52	3.27	0.008
	Line-contour	20.33	4.56	

4. Conclusion

We propose the innovative line-contour objectives and successfully demonstrate their feasibility. The optimal sources and relative aerial images have close similarities compared to that using a sigmoid model. According to the quantitative results of $DoPE_J$ and $DoPE_I$, source variations have insignificant impact to aerial images. Such merit allows the flexibility of converting complex sources to simple ones. The image fidelities measured by EPEs are close and so do NILSs that detect the image contrast. Moreover, the quadratic objective function enables a significant speed enhancement of CG. The consistent constants κ_1 between complexity and time ratios in both cases indicate our complexity analysis is accurate and quite independent of the masks. Furthermore, the E-D windows show similar process variation trends as being quantified by the standard deviation. Better elliptic E-D PWs are obtained by using our line-contour objectives, especially for the brick contact array. Our methodology is very promising for enhancing the speed of simultaneous SMO due to a simplification of the resist-image-based cost functions from nonlinear to quadratic.

Acknowledgments

This work was supported by National Science Council in Taiwan under grant number 96-2221-E-009-095-MY3 and partly by the TSMC-University joint development program.

#161845 - $15.00 USD Received 19 Jan 2012; revised 16 Mar 2012; accepted 16 Mar 2012; published 23 Mar 2012